Supplementary Information (SI) for Catalysis Science & Technology.

Supporting Information

Elucidation of the Factors Governing the Oxygen Evolution Reaction in $Ba_{0.5}Sr_{0.5}Co_xFe_{1-x}O_{3-\delta}$ Catalysts via *Operando* Hard and Soft X-ray Absorption Spectroscopy

Weijie Cao,[a†] *Mukesh Kumar,*[*a†] *Neha Thakur,*[a] *Mitsuhiro Matsumoto,*[b] *Yoichiro Tsuji,*[b] *Toshiki Watanabe,*[a] *Toshiyuki Matsunaga,*[a] *Yoshiyuki Kuroda,*[c] *Shigenori Mitsushima,*[c,d] *Yoshiharu Uchimoto*[a]

[a] Graduate School of Human and Environmental Studies, Kyoto University, Yoshida Nihonmatsu-cho, Sakyo-ku, Kyoto 606-8501, Japan

[b] Office of Institutional Advancement and Communications, Kyoto University, Yoshida Honmachi, Kyoto 606-8501, Japan

[c] Graduate School of Engineering Science, Yokohama National University, 79-5, Tokiwadai, Hodogaya-ku, Yokohama, Kanagawa, 240-8501, Japan

[d] Institute of Advanced Sciences, Yokohama National University, 79-5, Tokiwadai, Hodogaya-ku, Yokohama, Kanagawa, 240-8501, Japan

[*] *Corresponding author: kumar.mukesh.5x@kyoto-u.ac.jp*

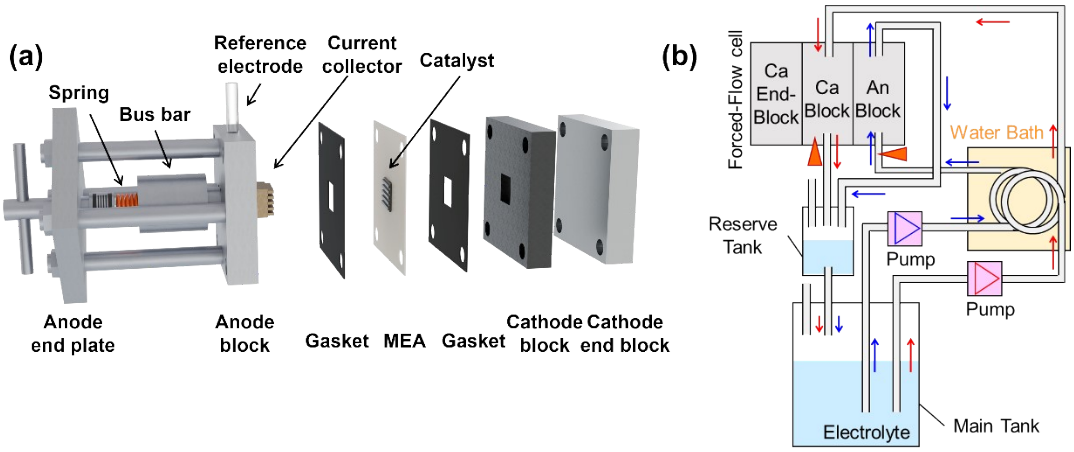

Fig. S1. Schematic representation of (a) side view of forced-flow cell and (b) experimental conditions.

Time-zero analysis

The standard three-electrode electrochemical cell struggles to measure OER activity accurately due to catalyst shedding and oxygen bubble formation. To address these issues, recent advancements have developed evaluation cells that secure the catalyst and control oxygen coverage by forcing electrolyte flow. This study introduced a new electrochemical measurement method, the "time-zero method," using a forced-flow cell (Fig. S2). This method determines catalytic activity by extrapolating from the initial time of bubble generation, providing kinetic current values under stable supersaturation and bubble-free conditions on the catalyst surface. By analyzing the 50-100 ms time region to eliminate the effect of double-layer charging current, a more accurate measurement of the true OER performance of the BSCF catalysts was achieved.

From this method, the decline in current due to bubbles generated on the catalyst layer is accounted for as a change in the diffusion-dominant current. The *Koutecký–Levich* equation, which models the measured electric current at an electrode from an electrochemical reaction in relation to the kinetic activity and the mass transport of reactants, is utilized as shown in the equation below.

$$\frac{1}{i} = \frac{1}{i_k} + \frac{1}{i_m}$$

In this case, *Cottrell* equation could be applied to obtain the mass transfer current density, as a function of time $i_m(t)$, as shown in equation, in which n, F, D and C are the reaction electron number, Faraday constant, diffusion coefficient, and concentration, respectively.

$$i_m(t) = \frac{nFACD^2}{\pi^{\frac{1}{2}} t^{\frac{1}{2}}}$$

Thus, the reciprocal of the current density i can be transformed into followed equation.

$$\frac{1}{i}=\frac{1}{i_k}+\frac{\pi^{\frac{1}{2}}}{nFCD^{\frac{1}{2}}}t^{\frac{1}{2}}$$

The inverse number of measured current $1/i$ is linear to $t^{1/2}$, and when time is 0, the predicted measured current is theoretically the same to the kinetic current.

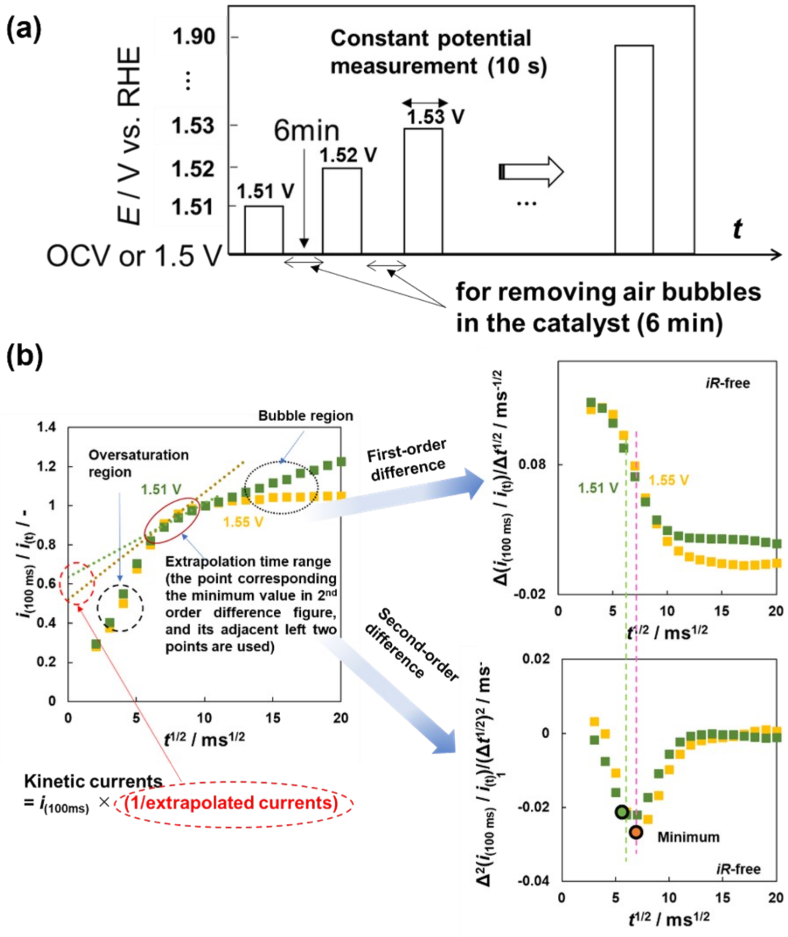

Fig. S2. (a) Pulsed potential step measurements. (b) Determination of extrapolation region.

The current change during the constant potential measurement could be divided in three parts. The first one is the charging of the electric double layer on the surface of catalysts, the second one is the generation of dissolved oxygen and formation of supersaturated layer in the electrolyte close to the surface of catalysts, and the third one is mass-transportation limitation due to the growth of oxygen bubbles. The third process was analyzed according to the Cottrell equation. The boundary of the second and the third parts is found as the point of larges curvature in the i^{-1}-$t^{1/2}$ curve. The point is also found as an inflection point in the first-order differential of the curve. It is mathematically well-known that the inflection point is found as the point in which the second-order differential value is minimum (It is equal to the point in which the third-order differential value is zero) in Fig. S2. The Y axis of $1/i_{(100ms)}$ is aiming to easily compare the i^{-1}-$t^{1/2}$ curves in one figure.

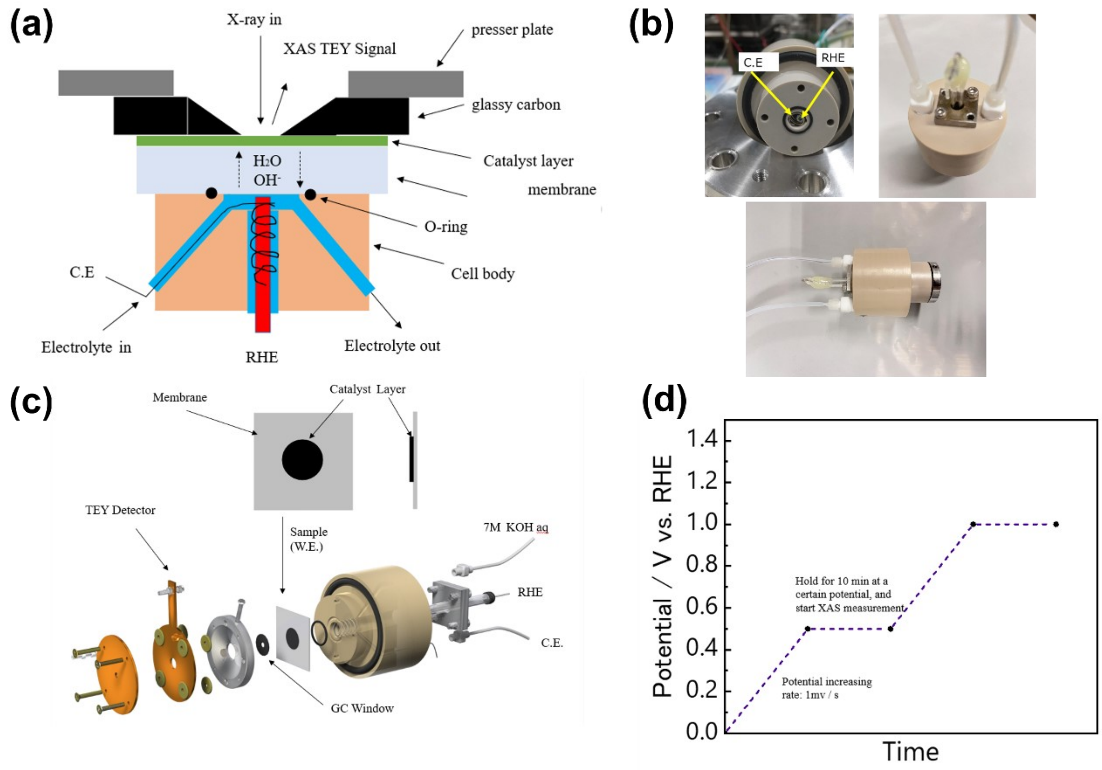

Fig. S3. (a) Sectional view, (b) practicality images and (c) decomposition chart of *operando* soft XAS cell. (d) *operando* XAS measurement procedure.

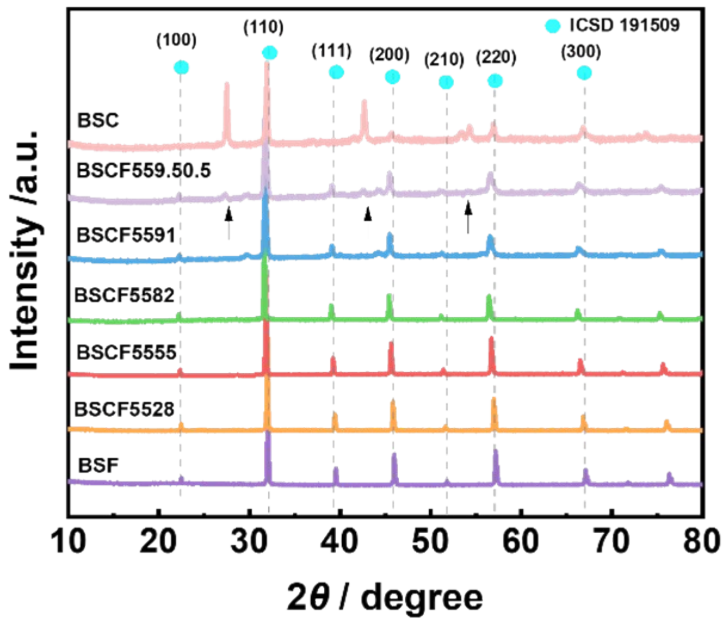

Fig. S4. (a) XRD patterns of $Ba_{0.5}Sr_{0.5}Co_xFe_{1-x}O_{3-\delta}$ (X=0, 0.2, 0.5, 0.8, 0.9, 0.95, 1.0).

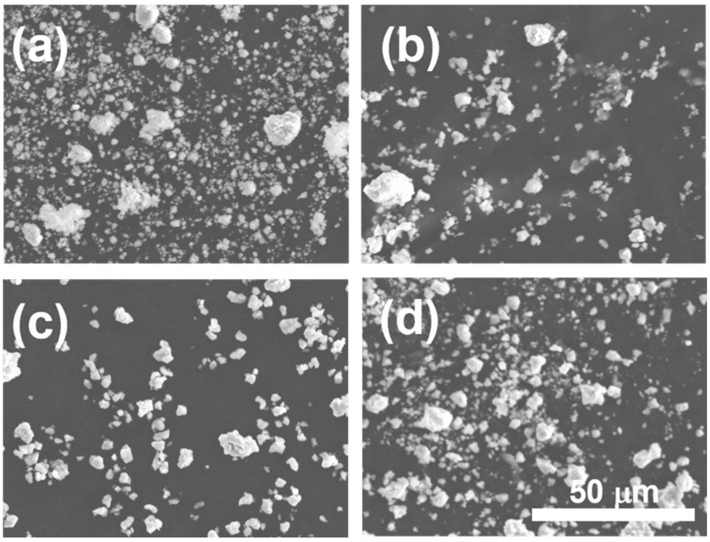

Fig. S5. SEM images of (a) BSC, (b) BSCF5582, (c) BSCF5528, and (d) BSF.

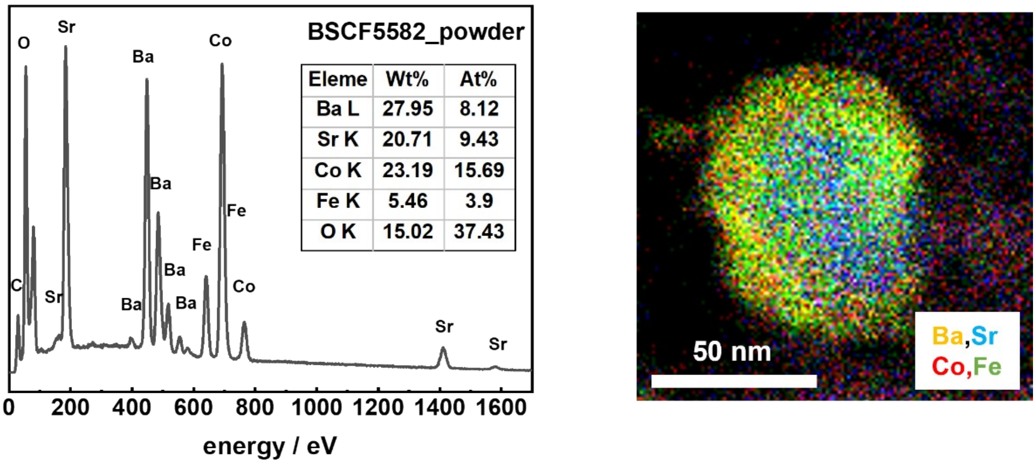

Eleme	Wt%	At%
Ba L	27.95	8.12
Sr K	20.71	9.43
Co K	23.19	15.69
Fe K	5.46	3.9
O K	15.02	37.43

Fig. S6. EDS spectra of BSCF5582 powder.

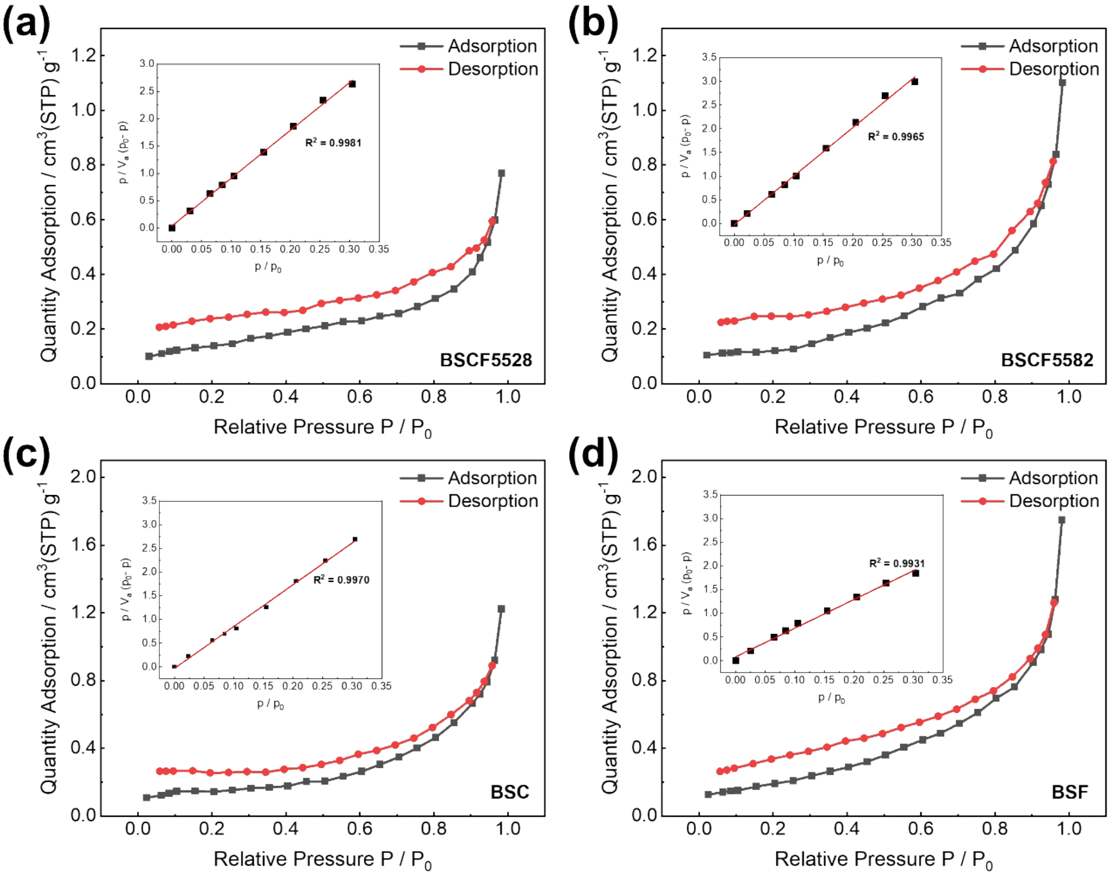

Fig. S7. Nitrogen adsorption/desorption isotherm patterns of (a) BSCF5528, (b) BSCF5582, (c) BSC, and (d) BSF.

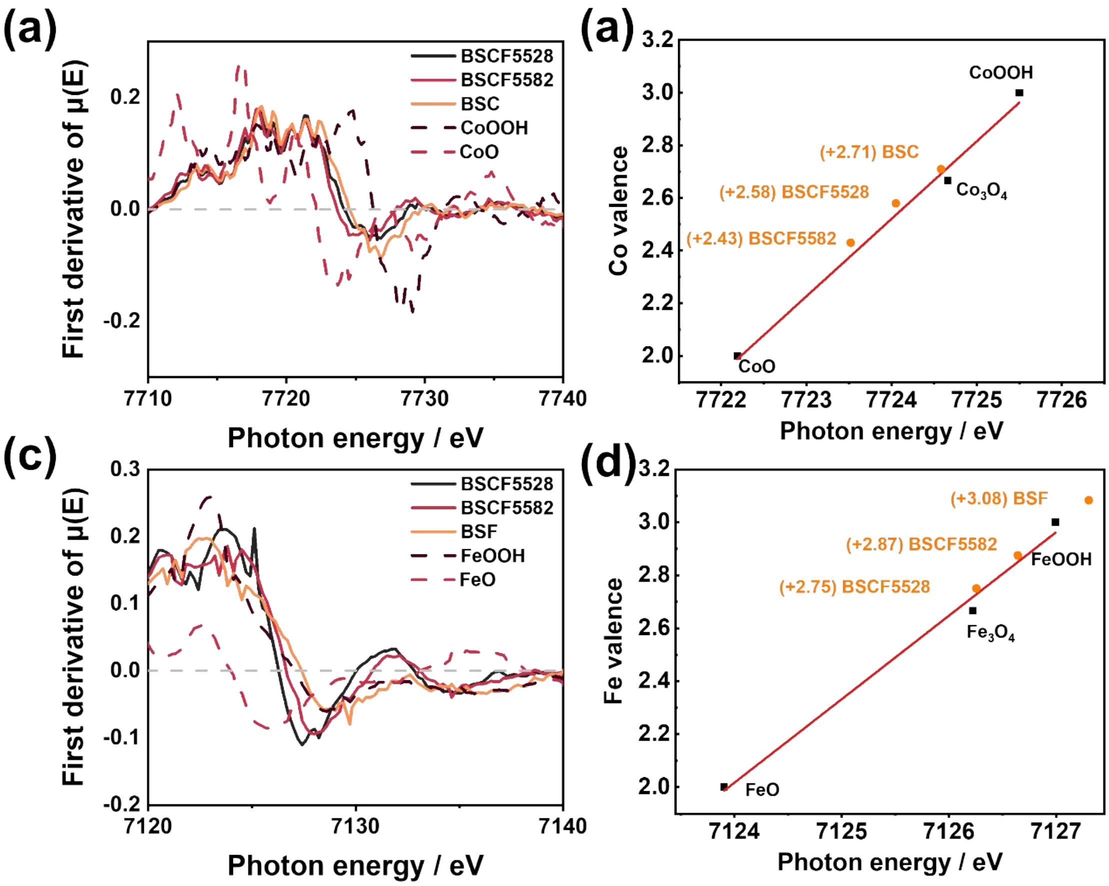

Fig. S8. (a) The first derivatives of the Co K-edge and (b) the fitted average oxidation states of Co. (c) The first derivatives of the Fe K-edge and (d) the fitted average oxidation states of Fe.

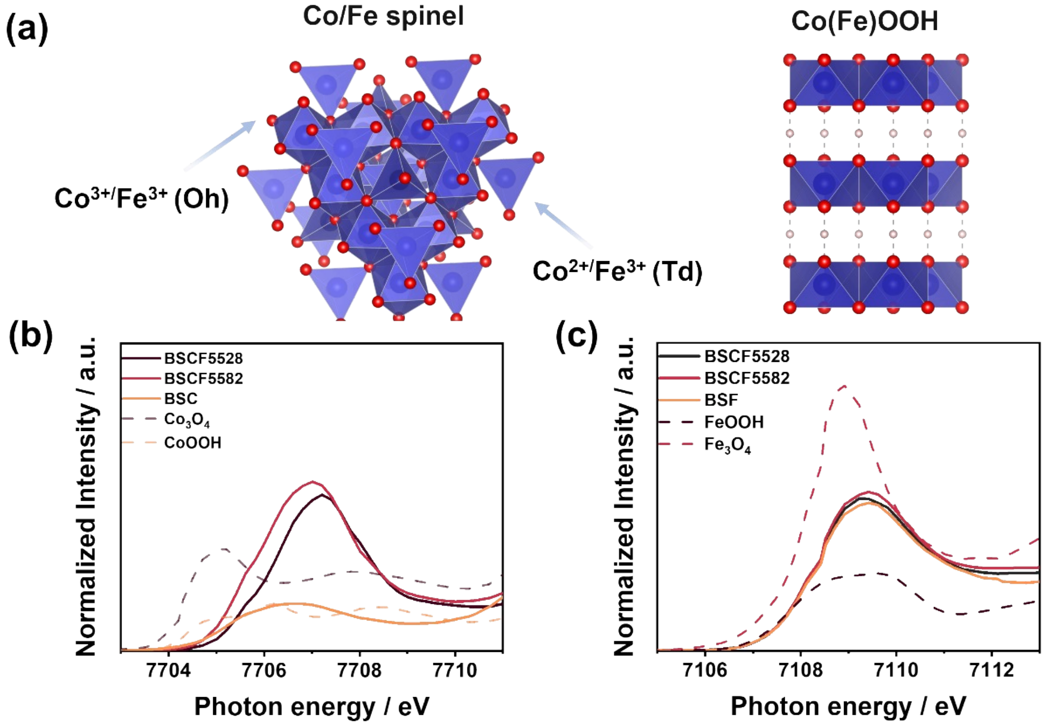

Fig. S9. (a) Presentation of Td and Oh site. An expanded view of the pre-edge part of the (b) Co and (c) Fe K-edge XANES.

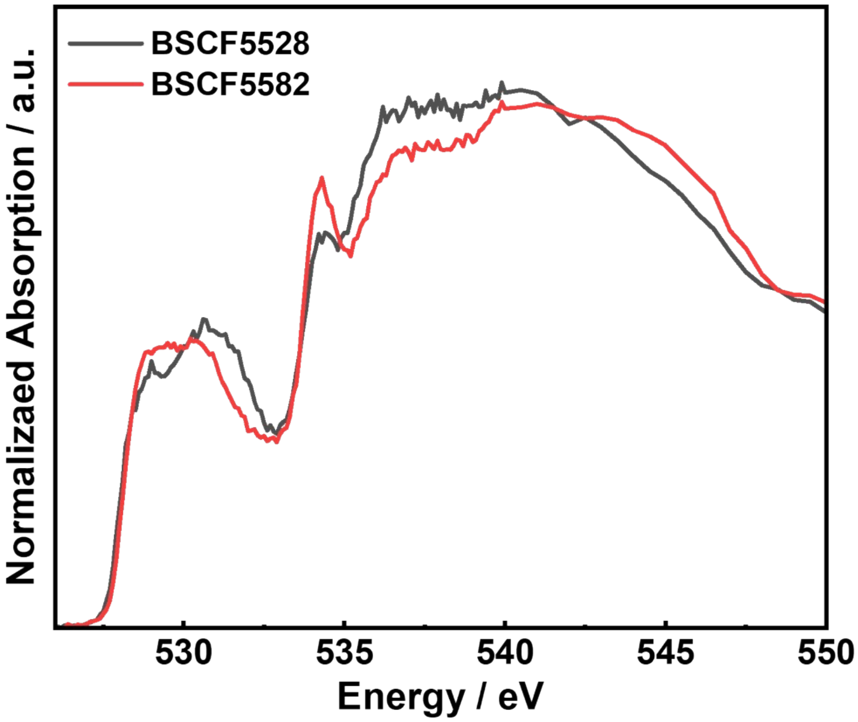

Fig. S10. O K-edge XAS spectra of BSCF5528 and BSCF5582.

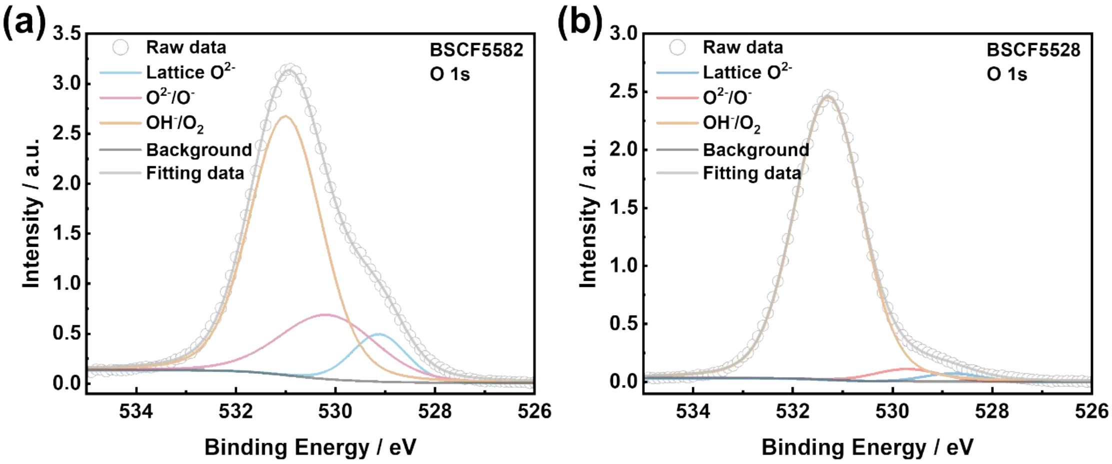

Fig. S11. XPS spectra of O 1s for (a) BSCF5582 and (b) BSCF5528.

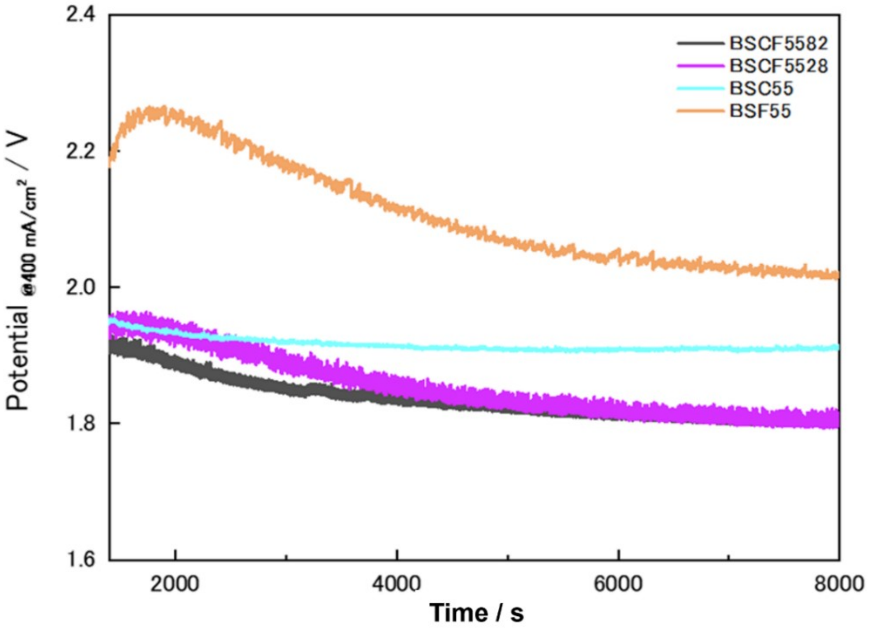

Fig. S12. Pre-treatment and activation of BSCF5582, BSCF5528, BSC and BSF by chronopotentiometry (CP) at 400 mA cm^{-2} recorded with forced flow cell.

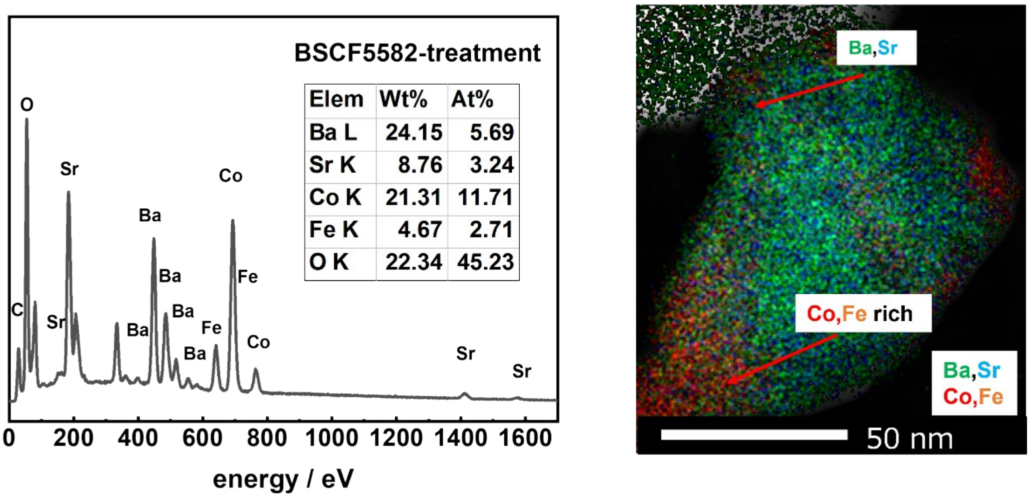

Elem	Wt%	At%
Ba L	24.15	5.69
Sr K	8.76	3.24
Co K	21.31	11.71
Fe K	4.67	2.71
O K	22.34	45.23

Fig. S13. EDS spectra of BSCF5582 after pre-treatment.

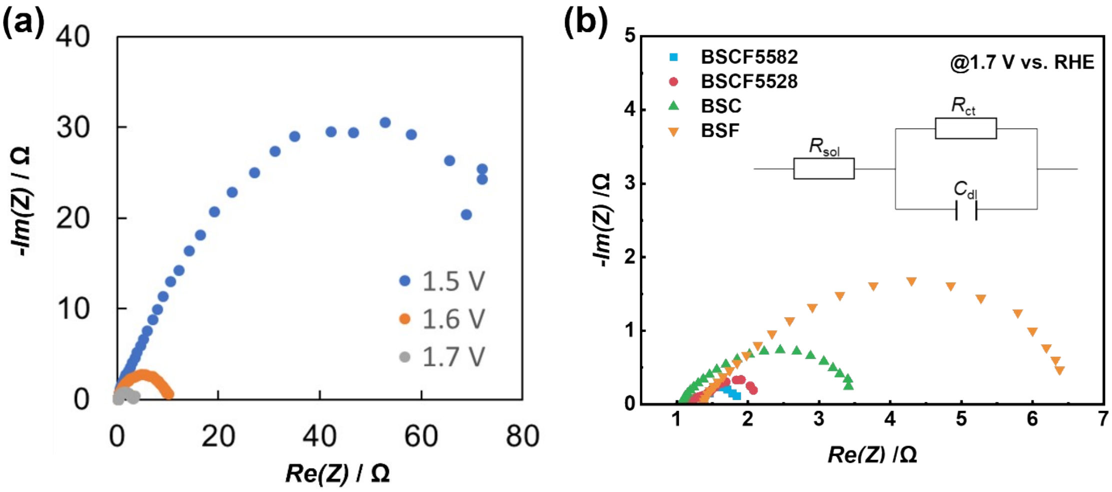

Fig. S14. (a) EIS plot of BSCF5582 at 1.5 V, 1.6 V and 1.7 V vs. RHE. (b) EIS plot of BSCF5582, BSCF5528, BSC and BSF at 1.7 V vs. RHE.

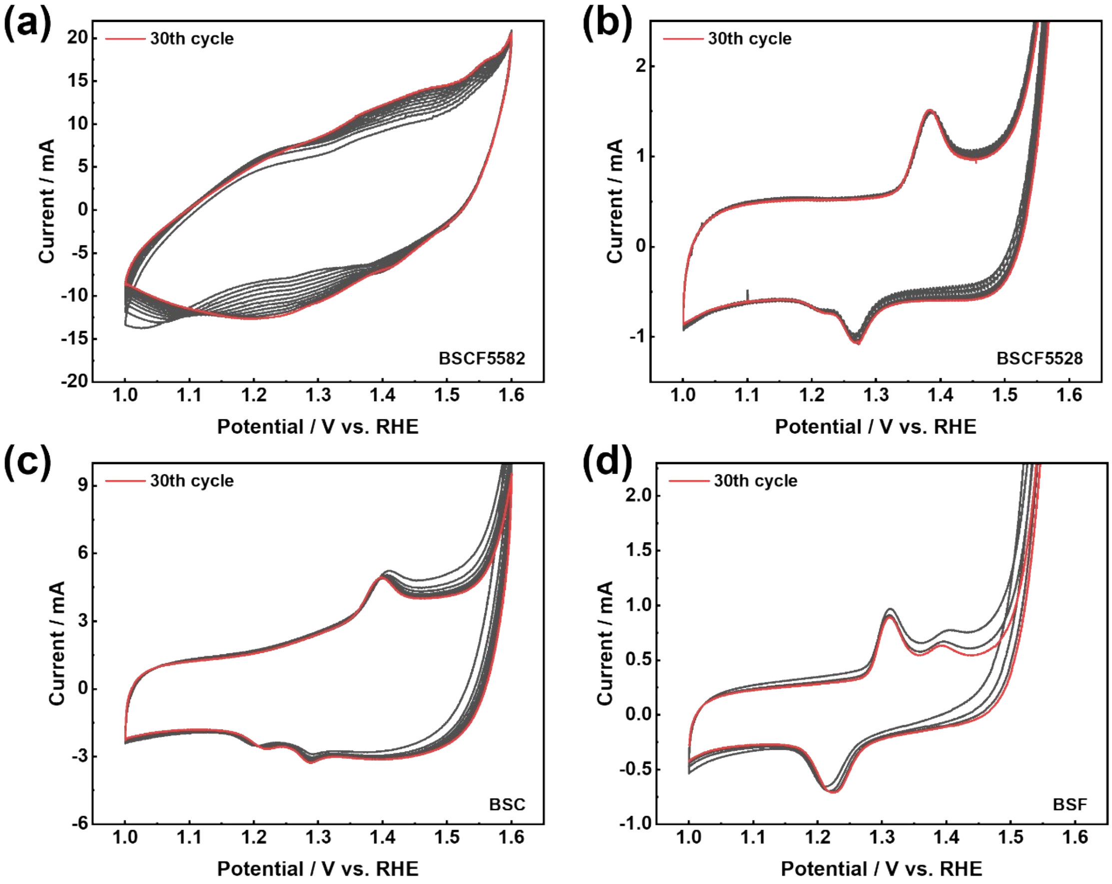

Fig. S15. CV curves for (a) BSCF5582, (b)BSCF5528, (c) BSC and (d) BSF catalysts during 1st to 30th cycles.

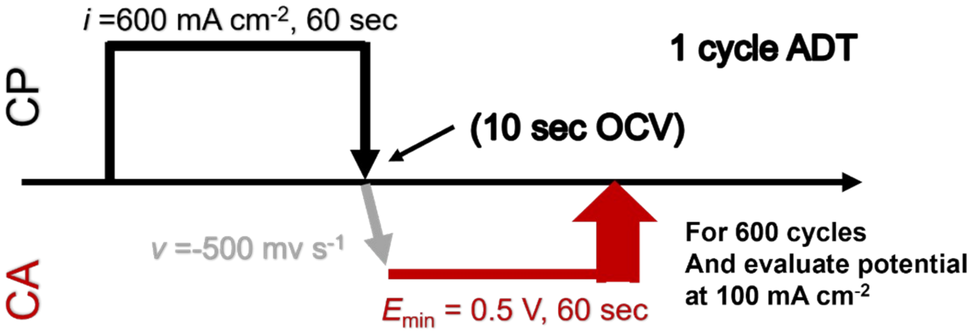

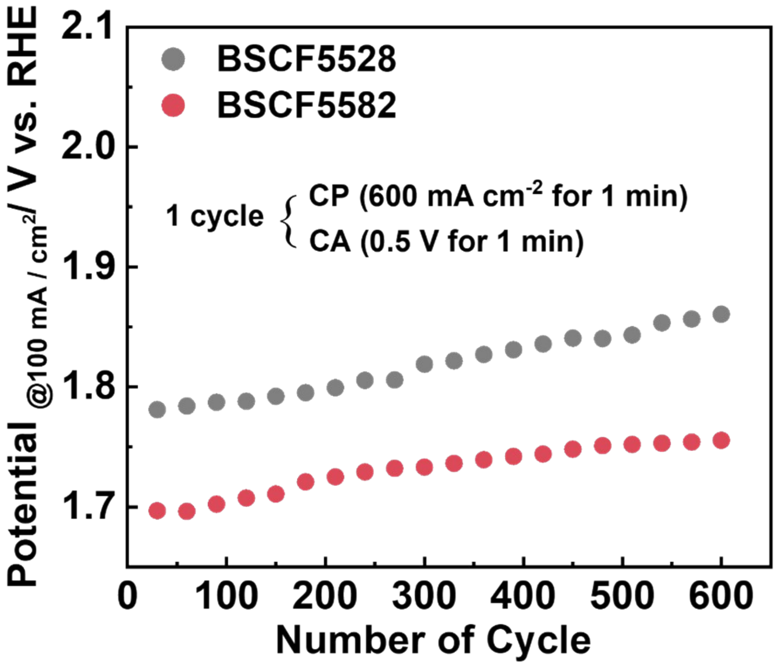

Fig. S16A. The anode potential corresponding to current density of 100mA cm^{-2} *vs.* ADT cycles of BSCF5528 and BSCF5582.

Electrochemical Surface Area (ECSA):

The ECSA is a critical parameter for evaluating catalyst performance as it is directly related to the number of available active sites. In this study, ECSA was determined based on the double-layer capacitance (C_{dl}). Cyclic voltammetry (CV) measurements were conducted within the non-faradaic potential window (1 to 1.05 V vs. RHE) in 0.1 M KOH, at scan rates ranging from 20 to 120 mV s^{-1}. The average current density (Ia+Ic)/2 @ 1.025 V was plotted against the scan rate, and the slope of the resulting linear fit was taken as C_{dl}. To calculate the ECSA, the obtained C_{dl} value was divided by the specific capacitance (C_s) of a flat surface, assumed to be 40 μF cm^{-2} in this work, consistent with values reported in the literature (typically between 20–60 μF cm^{-2}).[3]

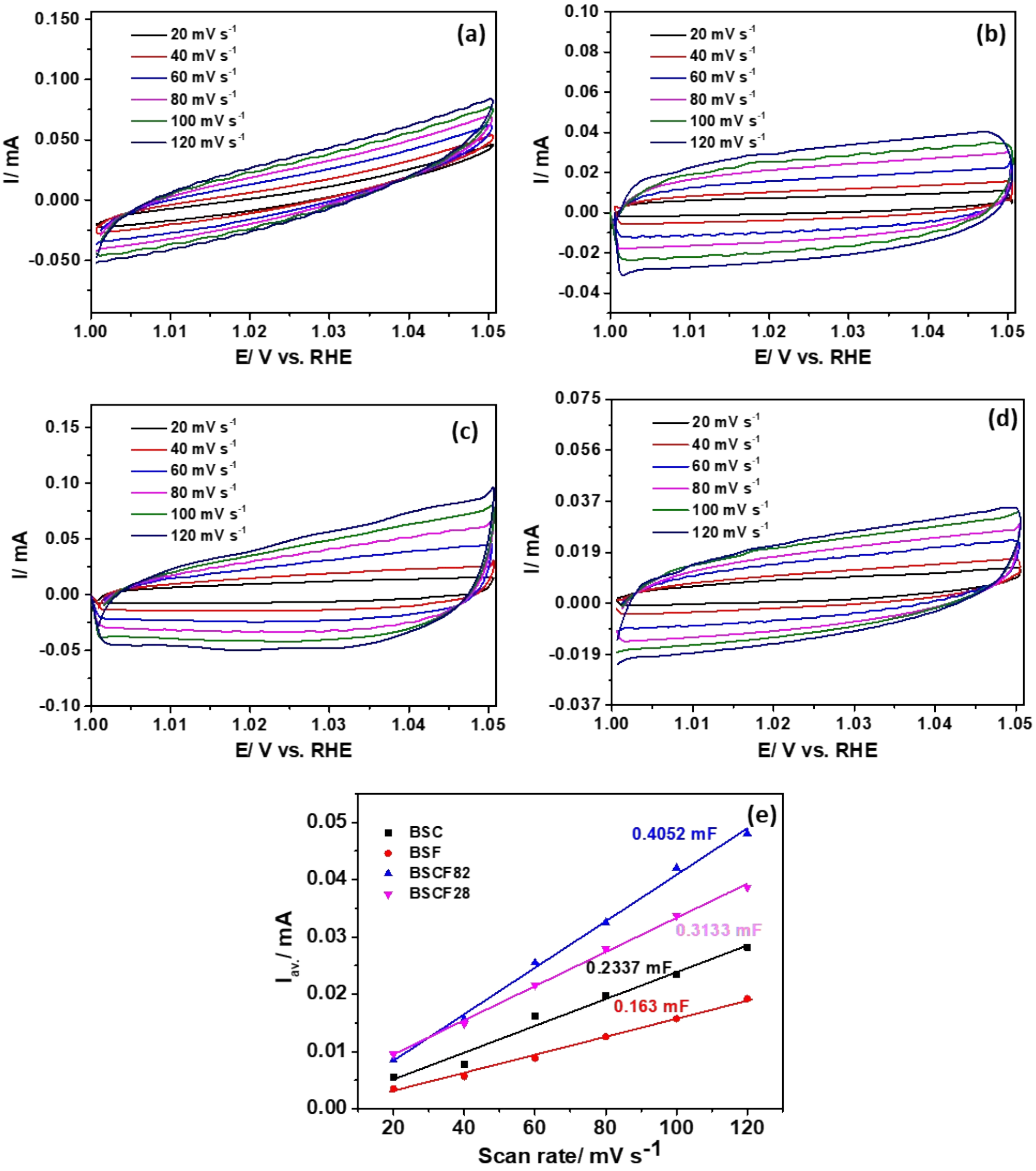

Figure 16B CVs curves of (a) BSC, (b) BSF, (c)BSCF82, (d) BSCF28 at various scan rates in the non-faradaic potential region. (e) corresponding average current versus scan rate plot.

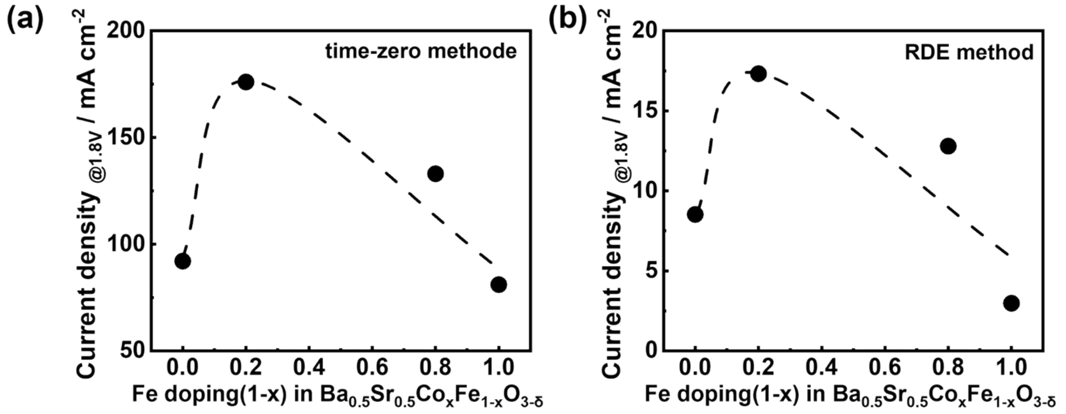

Fig. S17. Volcano-like relationship of Fe-doping and OER activity measured by (a) *time-zero* method and (b) RDE method.

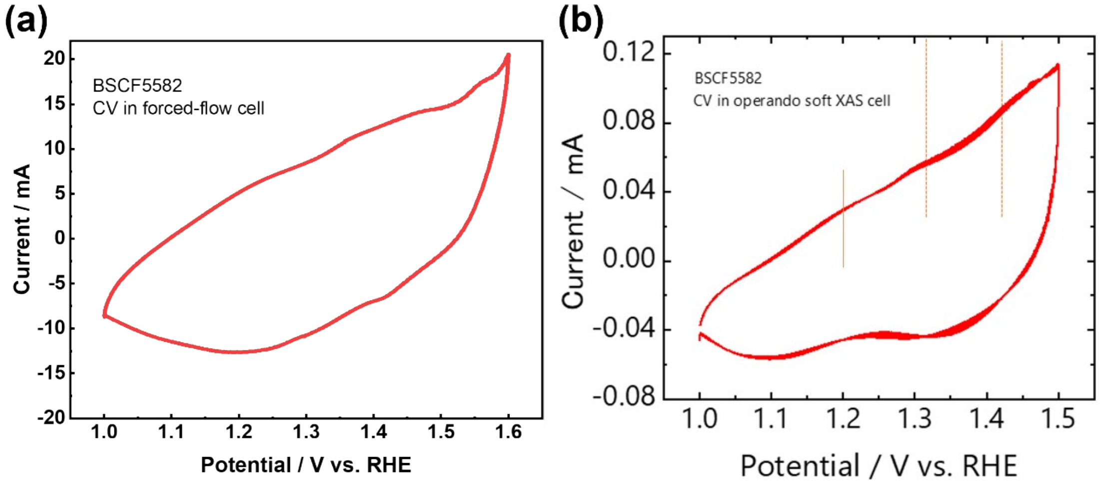

Fig. S18. CV comparison of BSCF5582 in (a) forced-flow cell and (b) *operando* soft XAS cell.

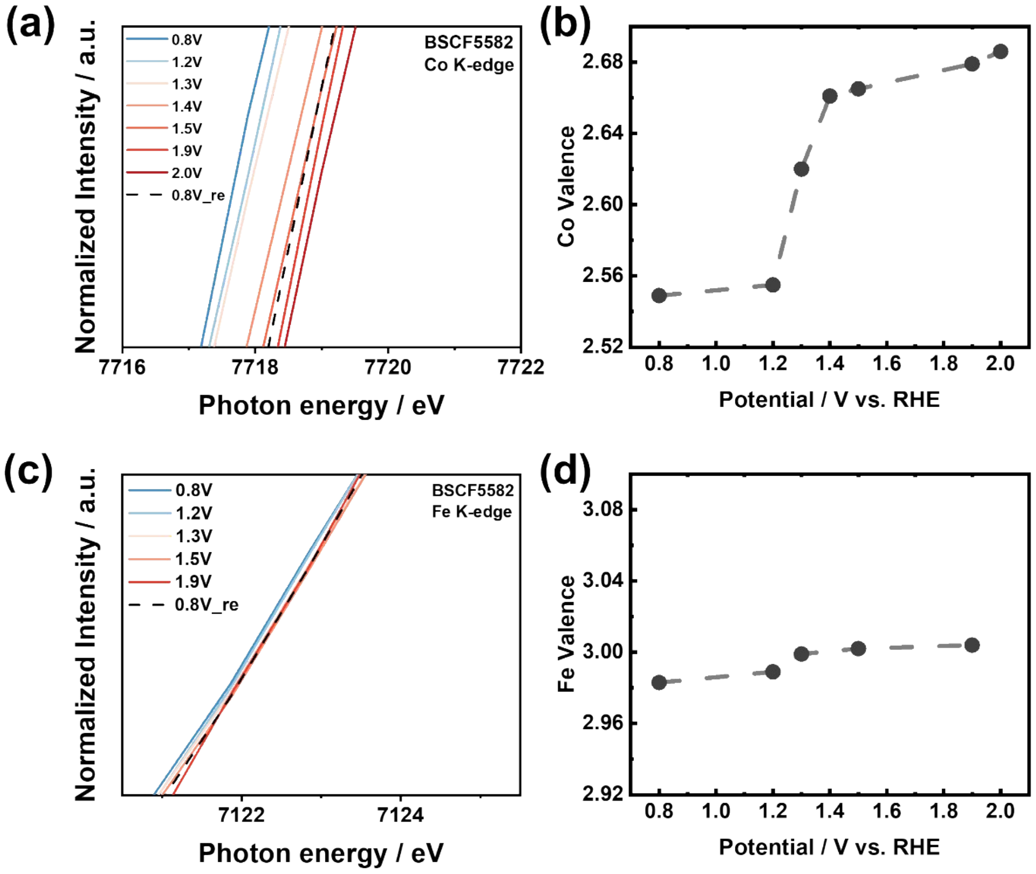

Fig. S19. (a) Co K-edge and (c) Fe K-edge of BSCF5582 during *operando* measurement. Fitted average oxidation states of (b) Co and (d) Fe.

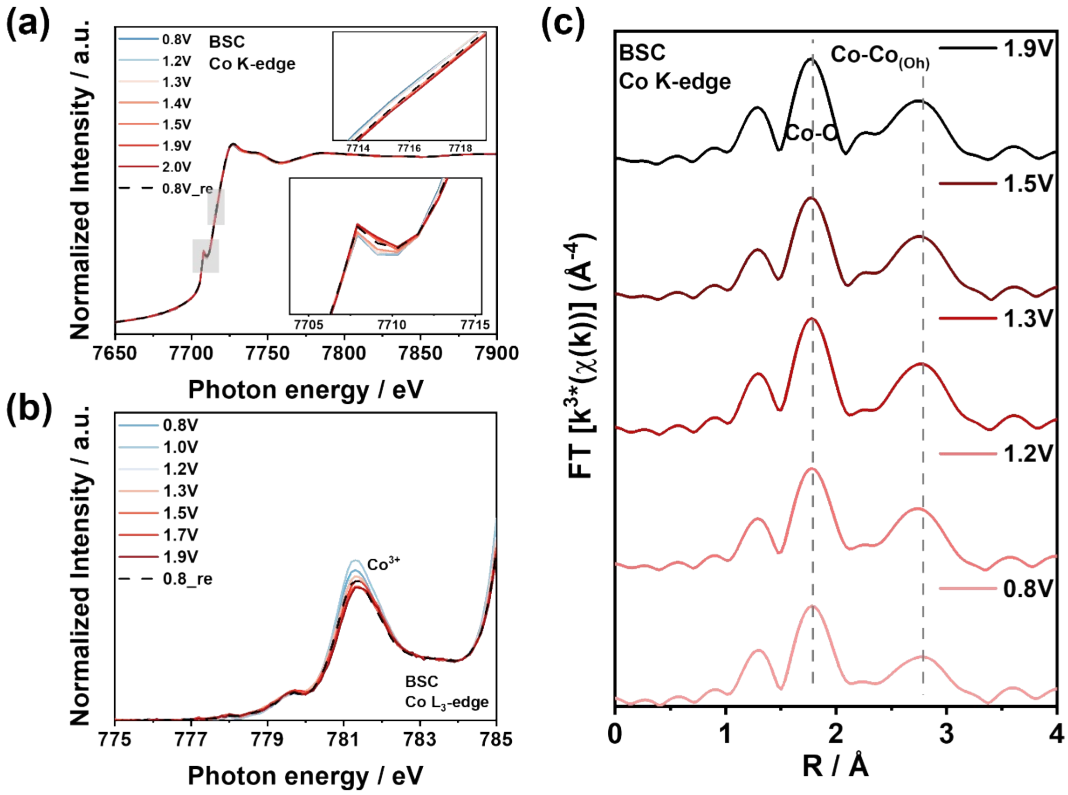

Fig. S20. *operando* XAS for investigating the origin of OER activity of BSC under application of catalytic potential from 0.8 V to 1.9 V vs. RHE. (a) Co K-edge XANES and (b) Co L-edge XANES spectra. (c) Fourier-transformed of the Co K-edge EXAFS spectra.

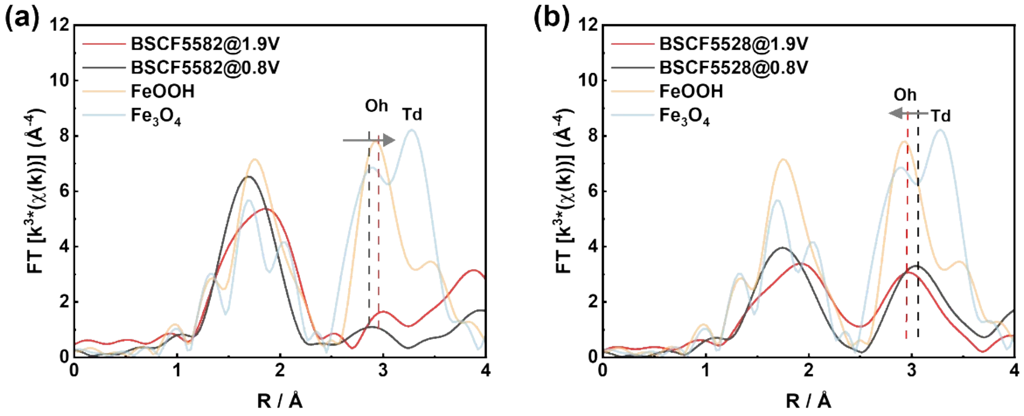

Fig. S21. (a) Fourier-transformed of the *operando* Fe K-edge EXAFS spectra of FeOOH, Fe_3O_4, BSCF5582 at 0.8 V and 1.9 V vs. RHE. (b) Fourier-transformed of the *operando* Fe K-edge EXAFS spectra of FeOOH, Fe_3O_4, BSCF5528 at 0.8 V and 1.9 V vs. RHE.

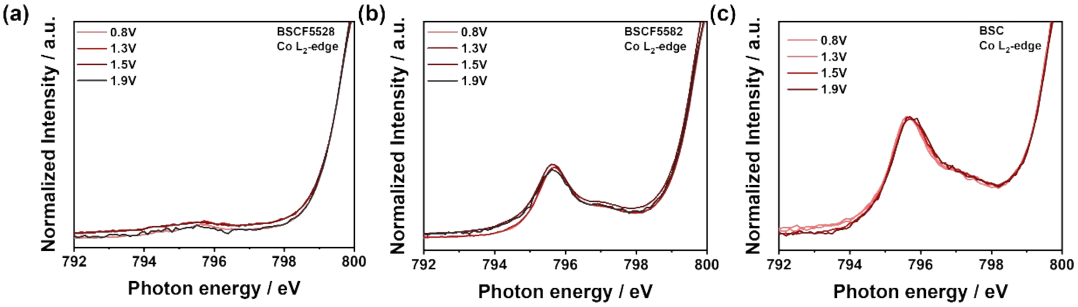

Fig. S22. *operando* Co L_2-edge XANES spectra of (a) BSCF5528, (b) BSCF5582, and (c) BSC.

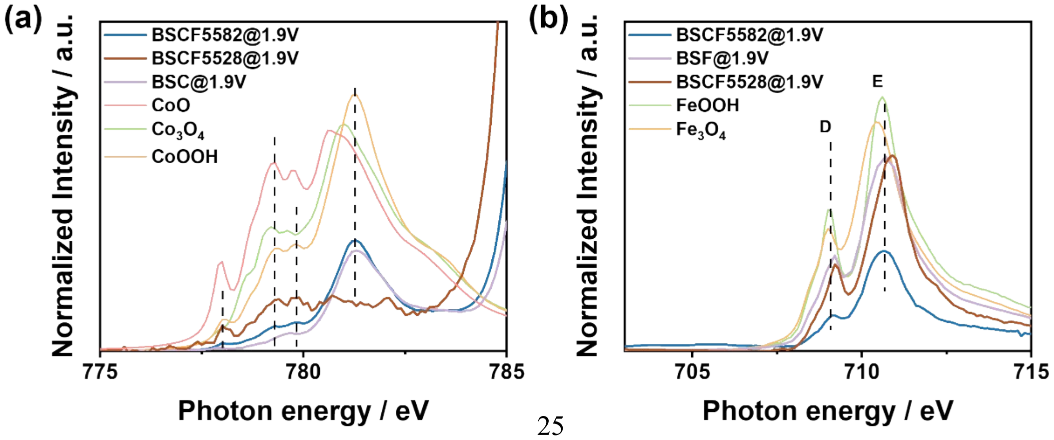

Fig. S23. (a) *operando* Co L_3-edge XANES spectra at 1.9 V vs. RHE of BSCF5528, BSCF5582, BSC, Co_3O_4, CoO and CoOOH. (b) *operando* Fe L_3-edge XANES spectra at 1.9 V vs. RHE of BSCF5528, BSCF5582, BSC, Fe_3O_4, and FeOOH.

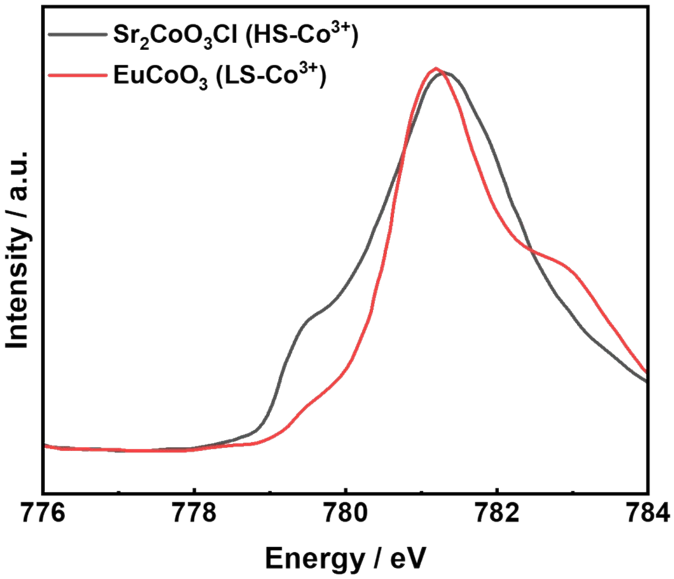

Fig. S24. Co L_3-edge XAS spectra of $EuCoO_3$ (LS-Co^{3+}), and Sr_2CoO_3Cl (HS-Co^{3+}) from Hu et al.[1]

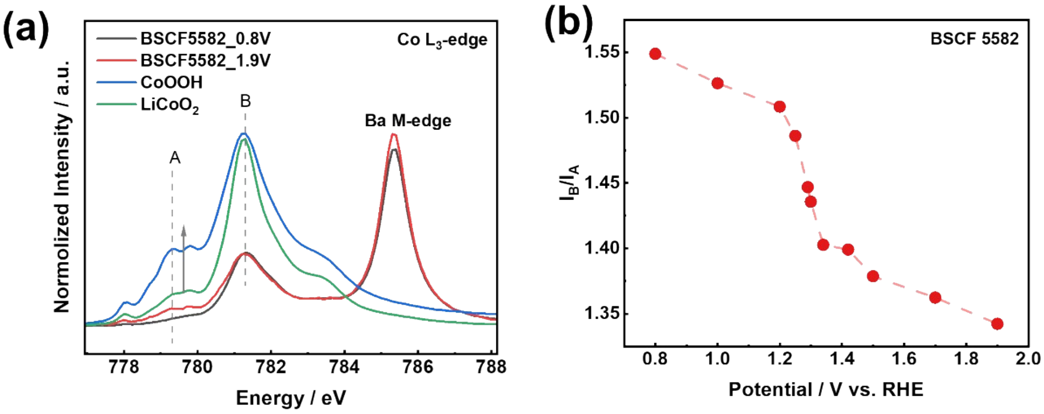

Fig. S25. (a) Co L_3-edge XAS spectra of BSCF5582 and (b) Corresponding peak intensity ratio between I_B and I_A in μ(E).

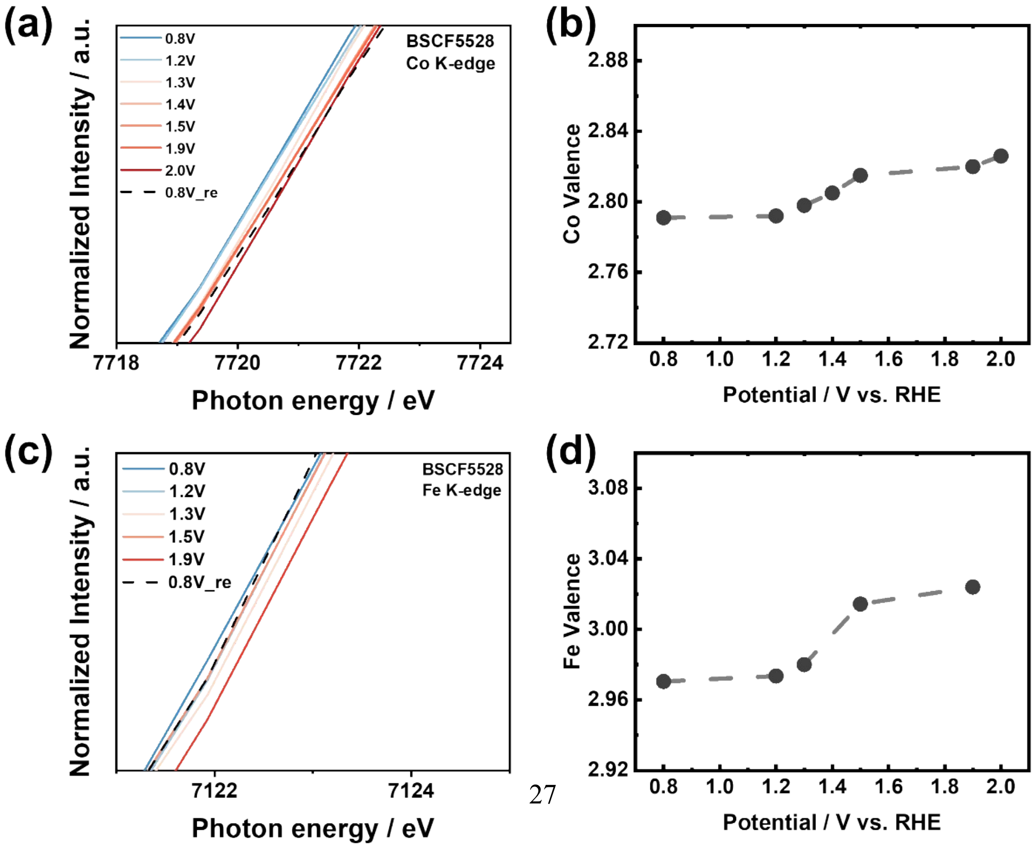

Fig. S26. (a) Co K-edge and (c) Fe K-edge of BSCF5528 during *operando* measurement. Fitted average oxidation states of (b) Co and (d) Fe.

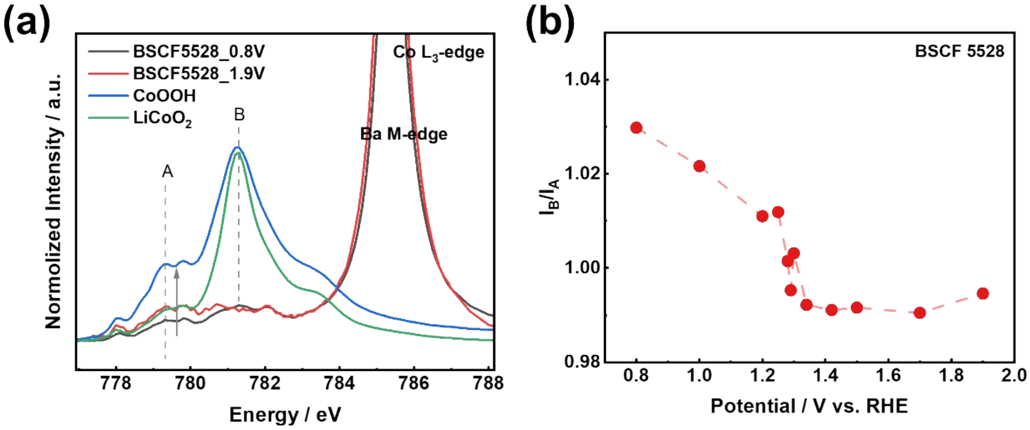

Fig. S27. (a) Co L_3-edge XAS spectra of BSCF5528 and (b) Corresponding peak intensity ratio between I_B and I_A in μ(E)

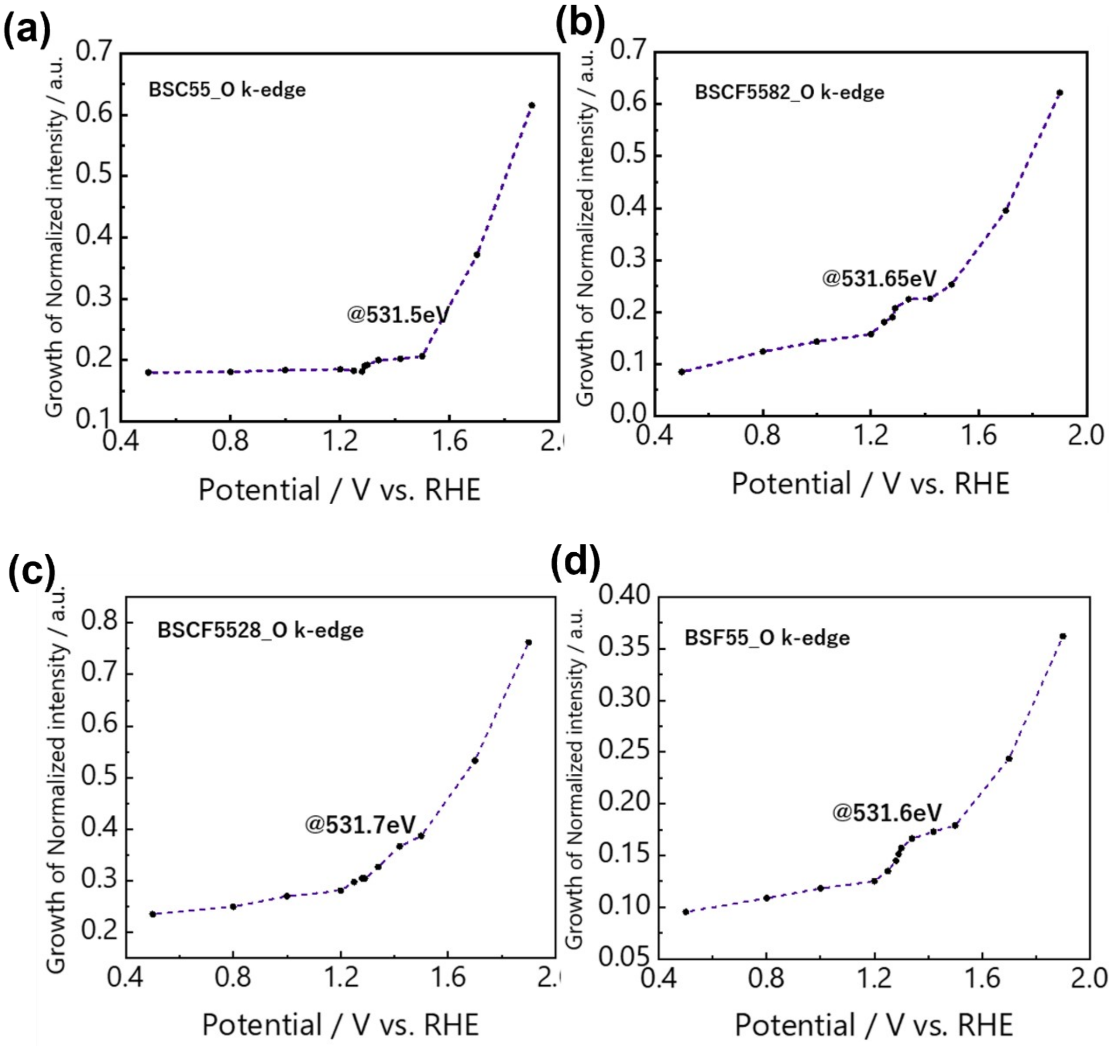

Fig. S28. Normalized *operando* O K-edge intensity growth with applied potential for (a) BSC, (b) BSCF5582, (c) BSCF5528 and (d) BSF.

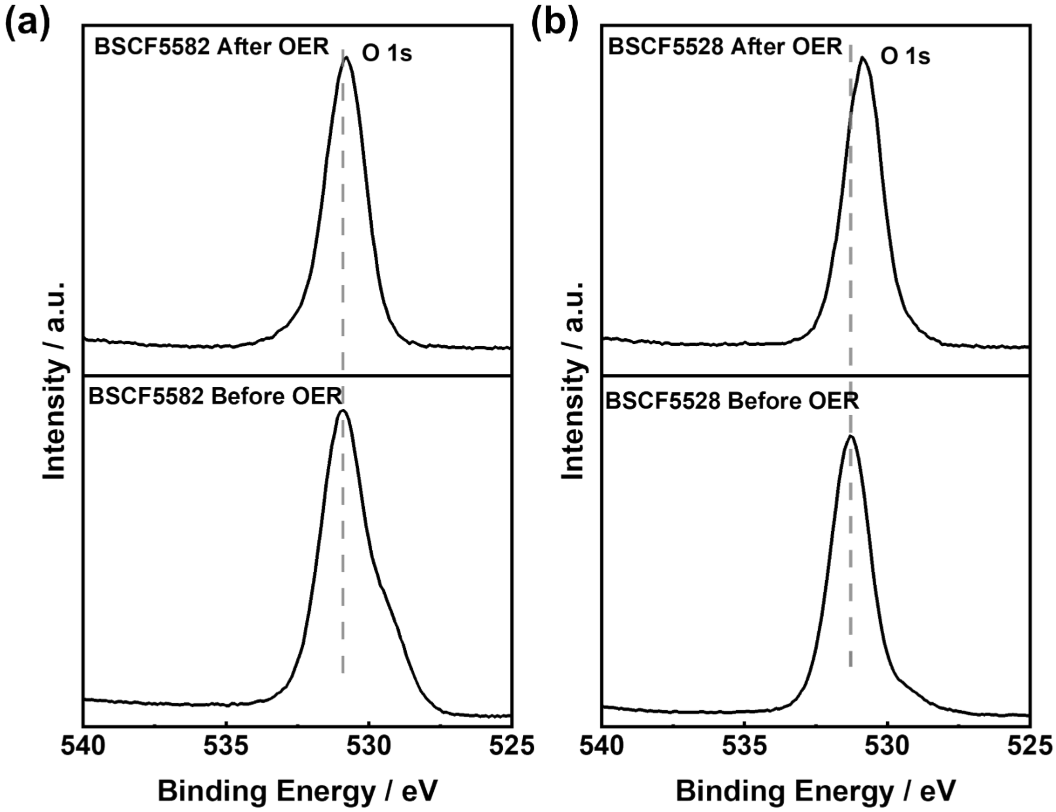

Fig. S29. O 1s XPS spectra of (a) BSCF5582 and (b) BSCF5528 before and after OER.

Table S1. Summarizing the abbreviations and their full forms used throughout the manuscript.

Abbreviation	**Full Form**
BSCF	$Ba_{0.5}Sr_{0.5}Co_xFe_{1-x}O_{3-\delta}$
BSC	$Ba_{0.5}Sr_{0.5}CoO_{3-\delta}$
BSF	$Ba_{0.5}Sr_{0.5}FeO_{3-\delta}$
BSCF5582	$Ba_{0.5}Sr_{0.5}Co_{0.8}Fe_{0.2}O_{3-\delta}$
BSCF5528	$Ba_{0.5}Sr_{0.5}Co_{0.2}Fe_{0.8}O_{3-\delta}$
OER	Oxygen Evolution Reaction
XAS	X-ray Absorption Spectroscopy
TEY	Total Electron Yield
RDE	Rotating Disk Electrode
EDS	Energy-dispersive X-ray Spectroscopy
XPS	X-ray Photoelectron Spectroscopy
XRD	X-ray Diffraction
BET	Brunauer–Emmett–Teller
TEM	Transmission Electron Microscopy
EXAFS	Extended X-ray Absorption Fine Structure
XANES	X-ray Absorption Near Edge Structure
LSV	Linear Sweep Voltammetry
CV	Cyclic Voltammetry
CA	Chronoamperometry
CP	Chronopotentiometry
EIS	Electrochemical Impedance Spectroscopy
Oh	Octahedral Coordination
Td	Tetrahedral Coordination
HS	High Spin
LS	Low Spin
μ_2-OH	Double Metal-coordinated Hydroxide Bridging Oxygen Sites
$\mu_{3/4}$-O	Threefold or Fourfold Metal-coordinated Oxygen Sites
BWNA	Bulk Water Nucleophilic Attack

Table S2A. Overpotential comparison of various perovskite electrocatalysts for OER at a current density of 10 mA cm^{-2}.

Catalyst	Electrolyte	Overpotential/mV	Ref.
$PrBa_{0.5}Sr_{0.5}Co_{1.5}Fe_{0.5}O_{5+\delta}$	1.0 M KOH	≈390	*Adv. Funct. Mater.* **2019**, *29*, 1901783
$Bi_{0.1}(Ba_{0.5}Sr_{0.5})_{0.9}Co_{0.8}Fe_{0.2}O_{3-\delta}$	0.1 M KOH	370	*Sci. Rep.* **2019**, *9*, 4210
$Sr(Co_{0.8}Fe_{0.2})_{0.7}B_{0.3}O_{3-\delta}$	0.1 M KOH	340	*Adv. Energy Mater.* **2019**, *9*, 1900429
$LaFe_{0.2}Ni_{0.8}O_3$	1.0 M KOH	302	*Angew. Chem., Int. Ed.* **2019**, *58*, 2316
$Ba_{0.9}Sr_{0.1}Co_{0.8}Fe_{0.1}Ir_{0.1}O_{3-\delta}$	0.1 M KOH	300	*ACS Appl. Energy Mater.* **2020**, *3*, 7149
$Ba_{0.5}Sr_{0.5}Co_{0.8}\text{-x}Fe_{0.2}Ni_{x}O_{3-\delta}$	0.1 M KOH	278	*Small* **2021**, *17*, 2006638
hexagonal $Ba_{0.5}Sr_{0.5}Co_{0.8}Fe_{0.2}O_{3-\delta}$	0.1 M KOH	360	*Inorg. Chem. Front.*, **2020**,*7*, 4488-4497
hexagonal $Ba_4Sr_4(Co_{0.8}Fe_{0.2})_4O_{15}$	0.1 M KOH	340	*Adv. Mater.* **2020**, *32*, 1905025
high-valence hybrid $Ba_{0.35}Sr_{0.65}Co_{0.8}Fe_{0.2}O_{3-\delta}$	0.1 M KOH	260	*Nat. Commun.* **2020**, *11*, 3376

Catalyst	Electrolyte	Overpotential/mV	Ref.
$Ba_{0.5}Sr_{0.5}(Co_{0.8}Fe_{0.2})_{0.9}O_{3-\delta}$	0.1 M KOH	290	*Nano Energy* **2022**, *99*, 107344,
$Ba_{0.5}S_{r0.5}Co_{0.8}Fe_{0.2}O_{3-\delta}$ mix $Gd_{0.2}Ce_{0.8}O_{1.9}$	0.1 M KOH	400	*Inorg. Chem.* **2023**, *62*, 10, 4373–4384
2H-type $B_{a1-x}Sr_xCoO_{3-\delta}$	0.1 M KOH	395	*Energy Fuels* **2022**, *36*, 6, 3219–3228
$Pr_{0.5}Sr_{0.5}Co_{0.8}Fe_{0.2}O_{3-\delta}$	0.1 M KOH	320	*ACS Appl. Energy Mater.* **2023**, *6*, 11, 6289–6298
$Ba_{0.5}Sr_{0.5}Co_{0.8}Fe_{0.2}O_{3-\delta}$ mix CeO_2	0.1 M KOH	290	*Green Chem.*, **2024**,*26*, 9433-9444
$Ca_3Co_4O_9$-$Ba_{0.5}Sr_{0.5}Co_{0.8}Fe_{0.2}O_3$	0.1 M KOH	389	*J Solid State Electrochem* **2024**, *28*, 3883–3891
RuO_2	**0.1 M KOH**	**465**	*ACS Appl. Energy Mater.* **2019**, *2*, 6, 4075–4083
IrO_2	**0.1 M KOH**	**366**	*ChemElectroChem* **2022**, *9*, e202200246.

Catalyst	Electrolyte	Overpotential/mV	Ref.
$Ba_{0.5}Sr_{0.5}Co_{0.8}Fe_{0.2}O_{3-\delta}$	**0.1 M KOH**	**390**	*Nat. Commun.* **2020**, *11*, 3376

Table S2B. Comparisons of Key Mechanistic Insight and techniques used for various perovskite electrocatalysts for OER.

Catalyst Composition	Key Mechanistic Insight	Techniques Used	Reference
high-valence hybrid $Ba_{0.35}Sr_{0.65}Co_{0.8}Fe_{0.2}O_{3-\delta}$	self-optimizing OER mechanism on hybrid BSCF evoked by pre-leaching of $BaCl_2$ and $SrCl_2$ during OER.	hard XAS, and soft XAS	*Nat. Commun.* **2020**, *11*, 3376
hexagonal $Ba_4Sr_4(Co_{0.8}Fe_{0.2})_4O_{15}$	Tetrahedral Co ions and octahedral O ions on the surface are active sites	Combined ex-situ XAS and DFT studies	*Adv. Mater.* **2020**, *32*, 1905025
$Ba_{0.35}Sr_{0.65}Co_{0.8}Fe_{0.2}O_{3-\delta}$	dynamic self-reconstruction of the materials to form a metal oxy(hydroxide) active layer.	Operando hard XAS	*Nat. Mater* **2017**,*16*, 925–931.
$Ba_{0.35}Sr_{0.65}Co_{0.8}Fe_{0.2}O_{3-\delta}$	Co^{2+} /Fe^{3+} spinel-like surface promotes the formation of the highly active Co(Fe)OOHphase	TEM-based imaging/diffraction and electron energy-loss spectroscopy (EELS)	*J. Am. Chem. Soc.* **2020**, 142, 15876−15883

Catalyst Composition	**Key Mechanistic Insight**	**Techniques Used**	**Reference**
$Ba_{0.35}Sr_{0.65}Co_{0.8}Fe_{0.2}O_{3-\delta}$	High Fe-content stabilizes the surface Co^{2+}-atoms limiting the reconstruction process.	HARD XAS	***J. Mater. Chem. A*,** **2024,12,** 5156-5169
$PrBa_{0.5}Sr_{0.5}Co_{2-x}Fe_{x}O_{5+\delta}$	Correlation between B-site doping and OER performance	EX-Situ hard XAS	***J. Mater. Chem. A,*** **2022,10**, 2271-2279
$PrBa_{0.5}Sr_{0.5}Co_{1.5}Fe_{0.5}O_{5+\delta}$	Effects of oxygen vacancies on the OER activity	XPS, DFT and STM	*Adv. Funct. Mater.* **2019**, *29*, 1901783
$Ba_{0.9}Sr_{0.1}Co_{0.8}Fe_{0.1}Ir_{0.1}O_{3-\delta}$	A low-level dopant Ir increases the B-O and reduces cobalt valence that enhances OER activity	XPS, and DFT	*ACS Appl. Energy Mater.* **2020**, *3*, 7149
$Ba_{0.5}S_{r0.5}Co_{0.8}Fe_{0.2}O_{3-\delta}$ mix $Gd_{0.2}Ce_{0.8}O_{1.9}$	gadolinium-doped ceria oxide suppresses the segregation and dissolution of A-site elements in BSCF and increases stability	XPS, Raman, MD simulation	*Inorg. Chem.* **2023**, *62*, 10, 4373–4384
$Ba_{0.5}Sr_{0.5}CoxFe_{1-}xO_{3-}\delta$	At lower Fe conc. Fe occupies octahedral sites, push Co to tetrahedral sites, encouraging the formation of the active CoOOH	Ex-situ/operando hard Co and Fe- K edge and Co/Fe L-edge and O K-edge X-ray absorption	***This work***

Catalyst Composition	Key Mechanistic Insight	Techniques Used	Reference
	phase. Higher Fe concentrations stabilize Co^{3+} in octahedral sites, leading to FeOOH formation but lower activity	spectroscopy (XAS)	

Table S3. BET specific surface area of each sample.

Sample	$a_{S,BET}$ ($m^2\ g^{-1}$)
$Ba_{0.5}Sr_{0.5}CoO_{3-\delta}$	0.72
$Ba_{0.5}Sr_{0.5}Co_{0.8}Fe_{0.2}O_{3-\delta}$	0.45
$Ba_{0.5}Sr_{0.5}Co_{0.5}Fe_{0.5}O_{3-\delta}$	0.49
$Ba_{0.5}Sr_{0.5}Co_{0.2}Fe_{0.8}O_{3-\delta}$	0.49
$Ba_{0.5}Sr_{0.5}FeO_{3-\delta}$	0.56

Note 1. EXAFS fitting detail

1. Reference Spectra and Model Construction

First, $S_0{}^2$ was obtained by fitting the FT-EXAFS spectra of a Co/Fe-metal reference sample (N=12) and fixed to 0.8. The following CIF files were used to generate the fitting models (ICSD codes are provided in parentheses): CoOOH (22285), Co_3O_4 (27497), and FeOOH (239322). The unit cell parameters of the reference models are as follows:

CoOOH: $R\bar{3}m$, a=b=2.88 Å, c=13.04 Å

Co_3O_4: $Fd\bar{3}m$, a=b=c=8.056 Å

FeOOH: $Pnma$, a =3.06 Å, b=4.64 Å, c=10.06 Å

We first performed fits on the spectra of these reference compounds, as shown in Fig. S30 and Table S4.

For CoOOH and FeOOH, the k-range was [3.0, 14.0] $Å^{-1}$ and the R-range was [1.0, 3.0] Å.

For Co_3O_4, the k-range was [3.0, 14.0] $Å^{-1}$ and the R-range was [1.0, 3.2] Å.

For the k^3-weighted $\chi(k)$ curve used in fitting, the number of independent points (N_{ipt}) was calculated using:[2]

$$N_{ipt} = \frac{2\Delta k \times \Delta R}{\pi}$$

In the FT curves of CoOOH and FeOOH (N_{ipt} =11.5), two peaks were observed near 1.5 Å and 2.5 Å, corresponding to Co/Fe-O and Co/Fe-Co/Fe(Oh) paths. A two-shell structural model incorporating these scattering paths was used for fitting. The Debye-Waller factors (σ^2), coordination numbers (CN), interatomic distances (ΔR), and energy shifts (ΔE_0) were set as free parameters. The number of adjustable parameters ($N_{\mathrm{para})}$ was within this limit.

For Co_3O_4, three peaks were observed near 1.5 Å, 2.5 Å, and 3.5 Å, corresponding to Co-O, Co-Co(Oh), and Co-Co(Td) paths. Since N_{para}=12≈N_{ipt}=12.6, a shell-by-shell fitting strategy was adopted. First, the Co-O scattering path within the R-range [1.0, 2.0] Å was fitted ($N_{\mathrm{para(4)}} < N_{\mathrm{ipt(5.7)}}$). After obtaining ideal fitting results, the R-range was expanded to [1.0, 3.2] Å, fixing the Co-O scattering path parameters and simultaneously fitting Co-

Co(*Oh*) and Co-Co(*Td*) paths ($N_{\text{para(8)}} < N_{\text{ipt(12.6)}}$). This adjustment strategy can also involve fixing the CN or ΔR parameters of the Co-Co(*Oh*) or Co-Co(*Td*) paths, allowing fine-tuning of the Co-O scattering path to achieve the optimal fit.

The fitting results confirmed that the CIF files used for CoOOH (22285), Co_3O_4 (27497), and FeOOH (239322) matched well with the reference spectra and could be further applied to the *operando* analysis of BSCF samples.

2. Fitting Strategy

Operando Co K-edge:

During *operando* measurements, BSCF5582 undergoes a structural transition from Co(*Td*) to Co(*Oh*) (Fig. S31 and Table S5). A three-shell model incorporating Co-O, Co-Co(*Oh*), and Co-Co(*Td)* paths was used for fitting. Due to high noise levels at large k-values, the k-range was reduced to [3.0, 10.0] $Å^{-1}$, and the R-range was set to [1.0, 3.0] Å, resulting in N_{ipt}=8.9. Using a shell-by-shell fitting strategy, the Co-O path was first fitted ($N_{\text{para(4)}} < N_{\text{ipt(4.4)}}$) and fixed, followed by fitting Co-Co(Oh) and Co-Co(Td) paths ($N_{\text{para(8)}} < N_{\text{ipt(8.9)}}$).

For BSCF5528, the k-range was [3.0, 11.0] $Å^{-1}$ and the R-range was [1.0, 3.0] Å, yielding N_{ipt}=10.2. No significant Co(*Td*) signal was observed, and most Co ions remained in *Oh* sites. Including the Co-Co(*Td*) path in the model resulted in poor fitting quality and high DW factors. Therefore, this path was excluded in the revised analysis ($N_{\text{para(8)}} < N_{\text{ipt(10.2)}}$), resulting in high-quality fits (Fig. S32 and Table S6).

Operando Fe K-edge

For Fe K-edge EXAFS fitting, both samples incorporated Fe-O and Fe-Fe(*Oh*) paths from FeOOH. The k-range was [3.0, 10.0] $Å^{-1}$ and the R-range was [1.0, 3.0] Å, with N_{ipt}=8.9. Both shell-by-shell and multi-shell fitting strategies yielded consistent results, meeting the independent points constraint ($N_{\text{para}(8)} < N_{\text{ipt}(8.9)}$).

3. Discussion

In Table S5 and S6, the coordination number of Co-O ($CN_{Co–O}$) for both BSCF5528 and BSCF5582 increase with applied potential, indicating the development of additional Co–O coordination in Co-O(OH) species during the OER process. The changes in $CN_{Co–Co}$ values reflect the formation and evolution of Co–Co coordination shells. The two Co–Co peaks observed at approximately 2.87-2.89 Å and 2.96-2.99 Å correspond to Co-Co(*Oh*) and Co-Co(*Td*) coordination, denoted as CN_{Oh} and CN_{Td}, respectively. In BSCF5582, the growth of Co-O(OH) species during anodic polarization leads to an increase in CN_{Oh} and a decrease in CN_{Td}. The elongation of the Fe-O bond length from 1.92 to 2.01 Å is attributed to the formation of Fe-OH intermediates, while the increase in Fe-Fe(*Oh*) distance from 2.94 to 3.01 Å indicates a transition from Fe_3O_4 to FeOOH configuration. In contrast, BSCF5528 shows decreasing in the coordination numbers of Co-Co(*Oh*) during anodic polarization. Additionally, the shortening of the Fe-Fe(*Oh*) bond length from 3.11 to 3.00 Å suggests a partial transition of Fe^{3+} from Td to Oh sites, associated with the formation of FeOOH as the primary active site.

Table S4. The corresponding R space curve fitting results of Co and Fe K-edge for CoOOH, Co_3O_4 and FeOOH.

	Shell	**CN**	**R (Å)**	**σ^2 (Å^2)**	**ΔE_0 (eV)**	**R factor**
CoOOH	Co-O	6.3(2)	1.89(3)	0.003(1)	2(1)	0.012
	Co-Co(*Oh*)	6.3(4)	2.84(5)	0.005(2)	1(1)	

Co_3O_4	Co-O	4.5(9)	1.90(5)	0.003(1)	4(1)	0.004
	Co-Co(*Oh*)	7.9(8)	2.87(4)	0.007(3)	4(1)	
	Co-Co(*Td*)	2.5(3)	3.03(6)	0.001(1)	11(5)	
FeOOH	Fe-O	7.6(10)	1.95(2)	0.010(3)	-4(3)	0.009
	Fe-Fe(*Oh*)	2.7(5)	3.01(1)	0.003(1)	6(2)	

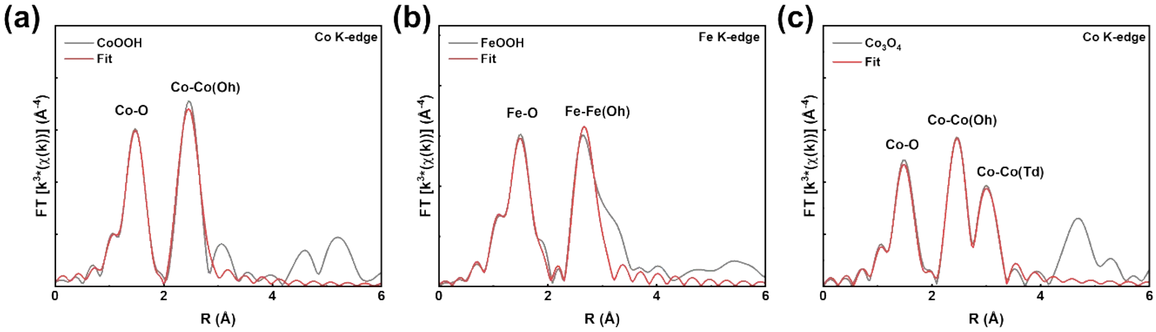

Fig. S30. Co and Fe K-edge EXAFS fitting curves in R-space of (a) CoOOH, (b) FeOOH, and (c) Co_3O_4.

Table S5. The corresponding R space curve fitting results of Co and Fe K-edge for the BSCF5582 catalysts varying different potential.

BSCF5582	**Shell**	**CN**	**R (Å)**	**σ^2 (Å^2)**	**ΔE_0 (eV)**	**R factor**
0.8 V	Co-O	3.4(3)	1.89(5)	0.008(2)	1 (1)	0.009
	Co-Co(*Oh*)	5.7(7)	2.90(1)	0.003(2)	12(5)	
	Co-Co(*Td*)	8.1(5)	3.01(2)	0.004(1)	7(2)	
1.9 V	Co-O	4.1(4)	1.86(6)	0.006(1)	-6(2)	0.004
	Co-Co(*Oh*)	6.2(2)	2.87(4)	0.003(2)	3(2)	

	Co-Co(*Td*)	3.9(6)	2.98(3)	0.001(1)	-11(3)	
0.8 V	Fe-O	3.9(4)	1.92(6)	0.004(2)	-7(2)	0.001
	Fe-Fe(*Oh*)	0.7(3)	2.94(3)	0.004(2)	-6(3)	
1.9 V	Fe-O	3.8(5)	2.01(8)	0.006(3)	6 (1)	0.016
	Fe-Fe(*Oh*)	2.5(9)	3.01(7)	0.010(3)	9(5)	

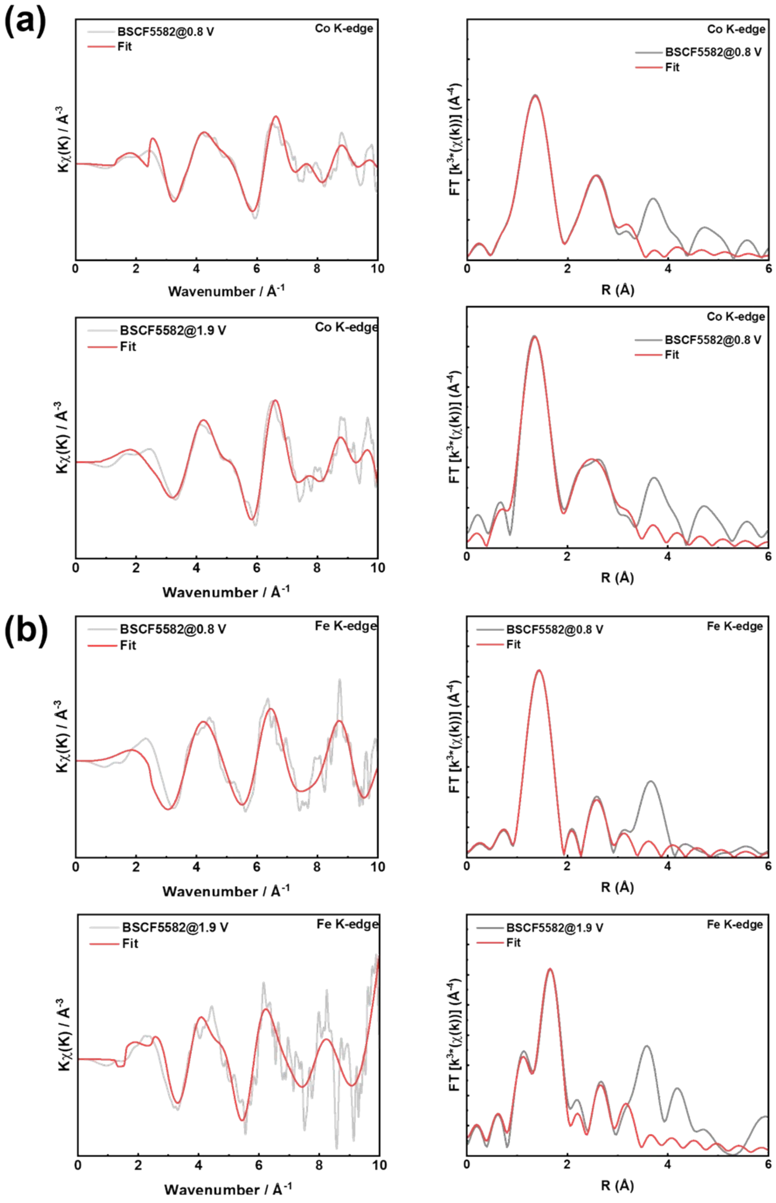

Fig. S31. Co and Fe K-edge EXAFS fitting curves in R-space and K-space for BSCF5582.

Table S6. The corresponding R space curve fitting results of Co and Fe K-edge for the BSCF5528 catalysts varying different potentials.

BSCF5528	**Shell**	**CN**	**R (Å)**	**σ^2 (Å^2)**	**ΔE_0 (eV)**	**R factor**
0.8 V	Co-O	3.7(2)	1.93(8)	0.007(3)	6(3)	0.019
	Co-Co(*Oh*)	9.2(5)	2.87(5)	0.010(5)	-3(2)	
1.9 V	Co-O	4.0(3)	1.94(5)	0.003(2)	6(3)	0.014
	Co-Co(*Oh*)	6.6(9)	2.88(3)	0.009(4)	-2(1)	
0.8 V	Fe-O	2.1(7)	1.93(4)	0.003(1)	-6(2)	0.014
	Fe-Fe(*Oh*)	1.5(7)	3.11(7)	0.006(1)	-2(1)	
1.9 V	Fe-O	2.8(3)	2.01(2)	0.005(3)	1(1)	0.001
	Fe-Fe(*Oh*)	3.5(5)	3.00(8)	0.011(2)	-3(1)	

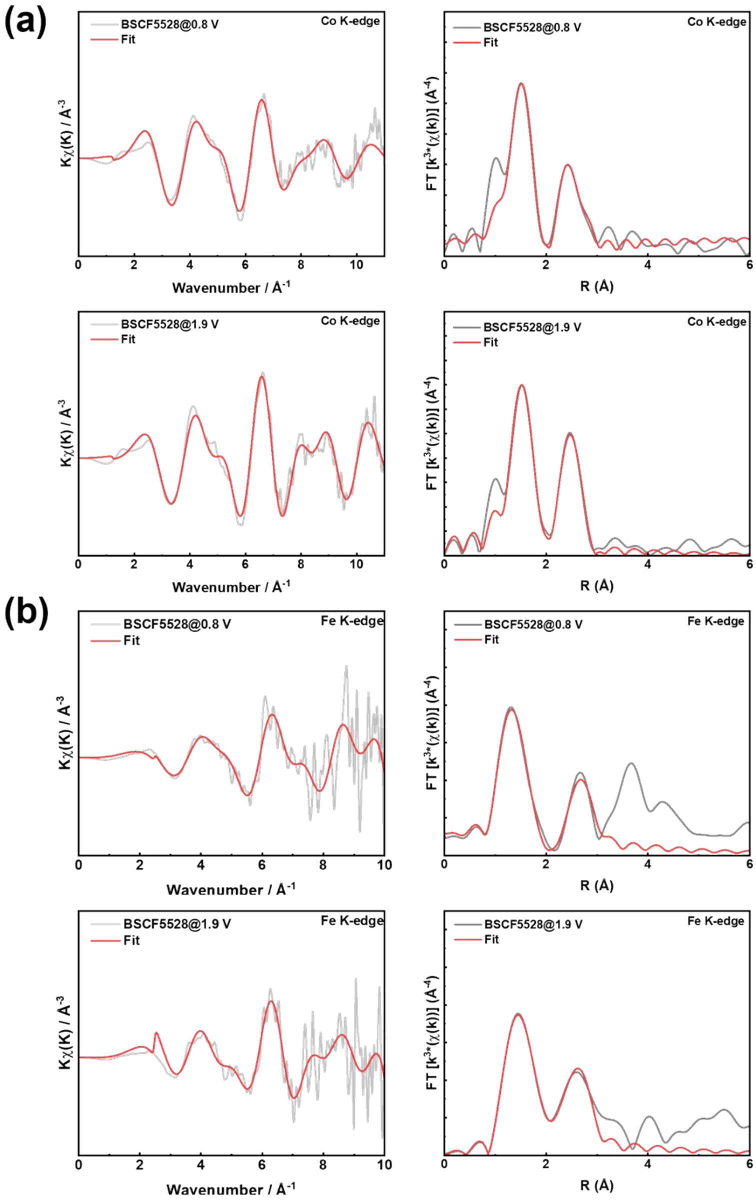

Fig. S32. Co and Fe K-edge EXAFS fitting curves in R-space and K-space for BSCF5528.

Reference

(1) Hu, Z.; Wu, H.; Haverkort, M. W.; Hsieh, H. H.; Lin, H. J.; Lorenz, T.; Baier, J.; Reichl, A.; Bonn, I.; Felser, C.; et al. *Phys. Rev. Lett.,* 2004, **92 (20)**, 207402.

(2) Li, S., Liu, T., Zhang, W. et al. *Nat Commun.* 2024, **15**, 3416.

(3) M. Kumar and T. C. Nagaiah, *J. Mater. Chem. A*, 2022, **10**, 7048-7057.